Journal of Applied Polymer Science

Study of carbonization behavior of polyacrylonitrile/tin salt as anode material for lithium-ion batteries

Haiying Wang, Xiu Zhang, Yaojie Zhang, Na Cheng, Tingyue Yu, Yang Yang, Gang Yang
Jiangsu Laboratory of Advanced Functional Material, Department of Chemistry, Changshu Institute of Technology, Changshu 215500, China
Correspondence to: G. Yang (E-mail: gyang@cslg.edu.cn)

Using polyacrylonitrile (PAN) as a template, a composite of tin salt/PAN nanofiber is facilely produced by an electrospinning technique. Under high-temperature heat treatment, the carbonization of PAN and the crystal growth of tin oxide proceed simultaneously to form a composite structure of tin nanoparticles wrapped in carbon nanofibers (tin@CNF). The composite structure of tin@CNF is controllable by the precursor ratio of PAN with tin salt and the carbonization temperature. The sample Sn1Pan1_700, synthesized from the precursor with weight ratio of $SnCl_2$:PAN = 1:1 and carbonized at 700 °C, delivers the initial capacity of 1329.8 mAh g^{-1} and remains at 741.1 mAh g^{-1} at the 40th cycle. The proper morphology of tin nanoparticles wrapped in carbon nanofibers plays an important role in specific capacity and cyclic performance, because the proper structure of carbon fiber hinders the aggregation of tin nanoparticles during the lithiation and delithiation processes. © 2016 Wiley Periodicals, Inc. J. Appl. Polym. Sci. **2016**, *133*, 43914.

KEYWORDS: composites; electrospinning; fibers

Received 27 December 2015; accepted 17 April 2016
DOI: 10.1002/app.43914

INTRODUCTION

Nowadays, rechargeable lithium-ion batteries (LIBs) are the most important storage power sources. The use of alloy materials as the anode of LIBs has attracted attention because of their advantages of high performance, low cost, safety, and so on.[1–3] However, severe volume changes have been reported in alloy anodes (during discharge and charge processes), inducing a rapid decay in stability.[4–6]

To minimize the volume change, three synthetic strategies have been suggested. (1) Synthesis of metal alloys with less active or inactive metal elements, such as Fe/Si, Co/Si, and Ni/Sn,[7–13] reduces the volume expansion during lithium alloying. Guo *et al.*[14] synthesized a microsize Si/Sn/Sb alloy composite by carbothermal reduction for a high-performance anode material. The multiphase characteristic of the Si/Sn/Sb alloy composite is considered to be a stable electrode. (2) Designing and fabricating nanostructures (such as nanowires or nanorods) can reduce the stress caused by the volume change.[15–22] For example, Yang *et al.*[23] reported superfine $Sn(SnSb)_{0.14}$ with improved cyclic performance. It was supposed that small particles have a stronger endurance to volume variation. Wang *et al.*[24] evaluated ZnO nanorod arrays for the negative electrodes of lithium-ion batteries. The array electrodes showed a stable capacity over 310 mAh g^{-1} after 40 cycles and good capacity retention as the anodes of lithium-ion batteries. (3) Embedding the active metal particles in a carbon matrix improves the cycleability of the metal anode. In metal/carbon composites,[25–32] the carbon matrix buffers the volume change and maintains good electronic contact with metal to improve cycleability. Yang *et al.*[28] synthesized silicon/carbon nanocomposites based on spray pyrolysis. The presence of silicon in the carbon matrix was shown to prevent pulverization and to improve the cycling stability of Si-based LIB anodes.

In our previous work, nanocomposites of Si/Sn nanoparticles and Sn nanoparticles wrapped in carbon fibers were synthesized and presented good capacity and improved cycle performance.[33,34] To the best of our knowledge, there are few reports modeling the relationship between the carbon fiber diameters and the size of the enwrapped nanoparticles. During the heat treatment, the carbonization of polyacrylonitrile and the crystal growth of tin nanoparticles proceed simultaneously. The diameter of fiber tends to be smaller, while the crystal size of tin tends to be larger. Tin nanoparticles with various particle sizes are wrapped in carbon nanofibers such that the composite structure of Sn@C is controllable under various heat-treatment conditions. The synergy between particle size and fiber diameters possibly plays the key role in the electrochemical performance. The proper diameter of carbon fiber and size of the particles would help improve the electrochemical performance.

In this work, a series of one-dimensional samples of tin nanoparticles wrapped in carbon nanofibers (CNF) were synthesized.

© 2016 Wiley Periodicals, Inc.

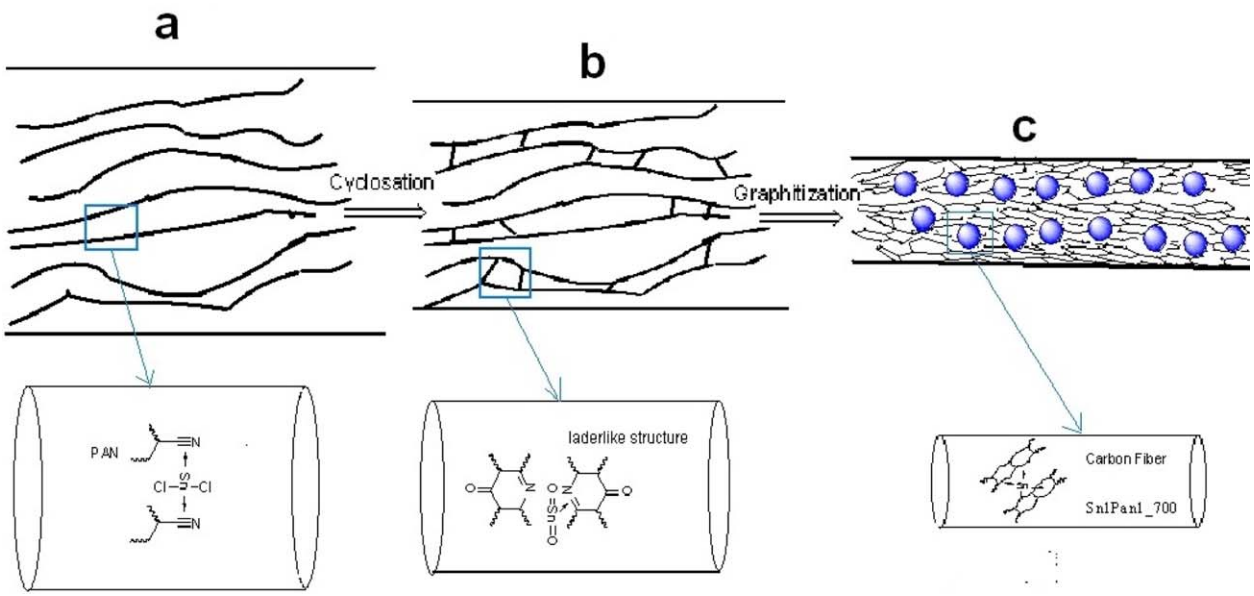

Figure 1. The schematic processes of Sn/carbon fibers from $SnCl_2$/PAN precursors: (a) $SnCl_2$ coexistence with linear PAN molecular chains, (b) SnO_2 coexistence with aromatic ladder structure PAN molecules during cyclization process, (c) carbonization of PAN and crystal growth of tin nanoparticles happen simultaneously. [Color figure can be viewed in the online issue, which is available at wileyonlinelibrary.com.]

The diameters of the carbon fibers and the size of the enwrapped nanoparticles are carefully modeled. The composites are characterized by X-ray diffraction (XRD), scanning and transmission electron microscopy (SEM and TEM), and Fourier transform infrared spectroscopy (FTIR) analysis. The relationship between the composite structure and the electrochemical performance of Sn@CNF is studied in detail.

EXPERIMENTAL

Polyacrylonitrile (PAN, $M_w = 150{,}000$) (Aldrich, Shanghai, P. R. China), stannic chloride ($SnCl_2$, 98%), and dimethylformamide (DMF) were used without further purification. In a typical procedure, the PAN solution (10 wt %) was prepared by dissolving PAN in the solvent of DMF under magnetic stirring for 12 h. $SnCl_2$ was slowly added to the PAN solution and stirred for 6 h

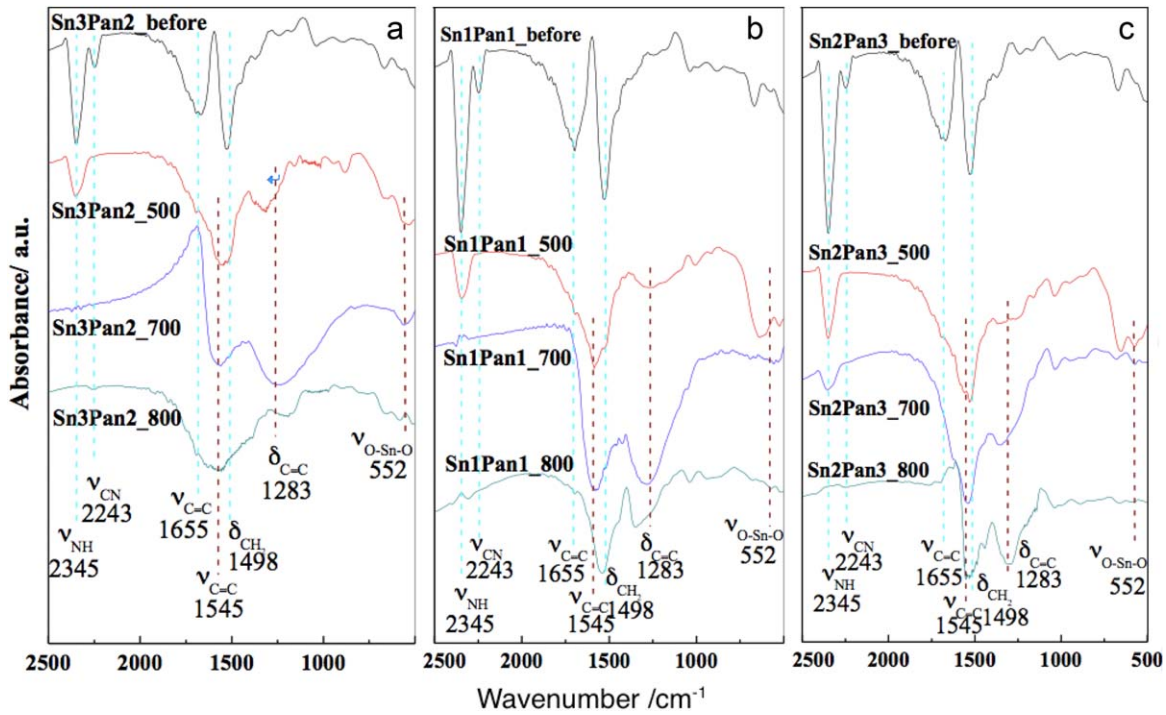

Figure 2. FTIR spectra of (a) Sn3Pan2, (b) Sn1Pan1, and (c) Sn2Pan3. The samples with three heat-treatment temperatures are listed in the figures. [Color figure can be viewed in the online issue, which is available at wileyonlinelibrary.com.]

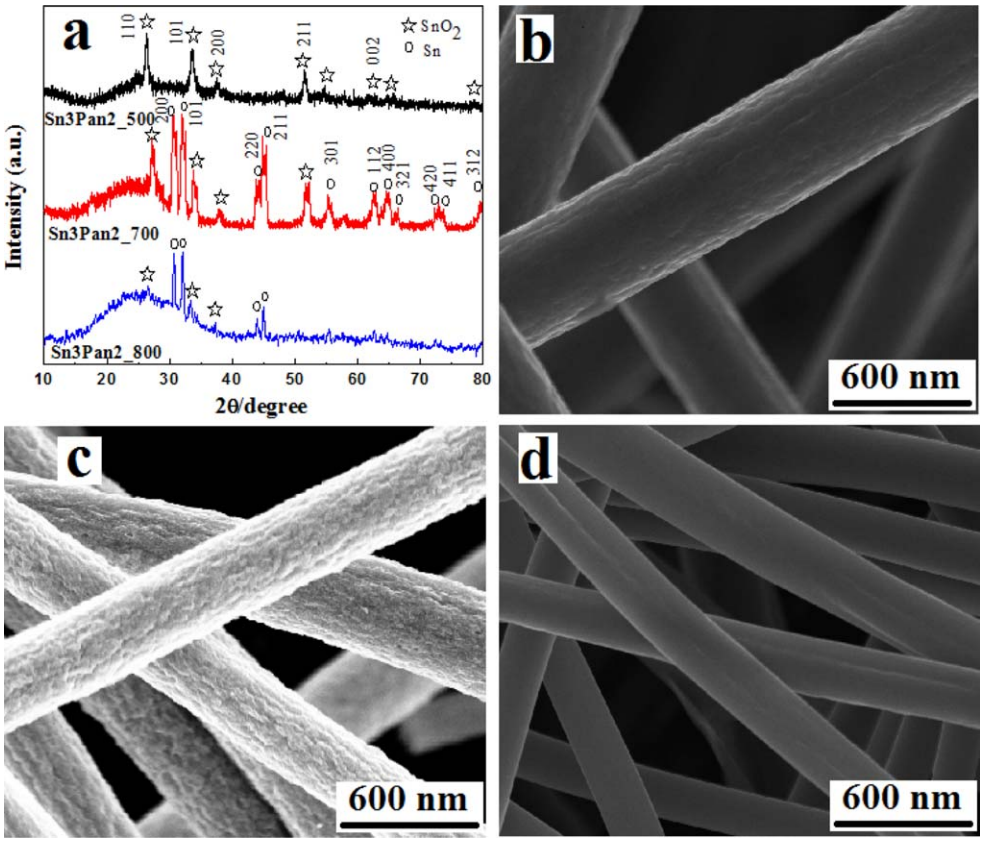

Figure 3. (a) XRD patterns, and SEM images of (b) Sn3Pan2_500, (c) Sn3Pan2_700, and (d) Sn3Pan2_800. [Color figure can be viewed in the online issue, which is available at wileyonlinelibrary.com.]

to obtain the mixed solution. The resulting solution was held in a spinning nozzle with a tip diameter of 1 mm, and a copper pin was connected to the anode of a high-voltage generator. The working high voltage was fixed at 20 kV, and the distance between the needle and aluminum foil collector was fixed at 12 cm. After the electrospinning process, a white color film of $SnCl_2$/PAN was obtained. The weight ratios of precursor $SnCl_2$ and PAN were 2:3, 1:1, and 3:2, and thus the obtained samples were simply named as Sn2Pan3, Sn1Pan1, and Sn3Pan2, respectively.

The white film of $SnCl_2$/PAN was heated at 250 °C for 1 h under air atmosphere, and a black film of tin oxide/PAN was obtained. The black film was subsequently heated in N_2 atmosphere at a temperature of 500, 700, or 800 °C for 3 h. Based on the heating temperature, the samples were named Sn2Pan3_500, Sn1Pan1_500, Sn3Pan2_500, Sn2Pan3_700, Sn1Pan1_700, Sn3Pan2_700, Sn2Pan3_800, Sn1Pan1_800, and Sn3Pan2_800.

By using a Rigaku (Rigaku Corporation, Japan) diffractometer with Cu K_α radiation, XRD patterns were collected at a 0.02° step width from 10° to 80°. The lattice parameters and the average crystal size of nanoparticles were refined and calculated using MDI Jade software (FESEM, SIGMA, ZEISS microscope, Germany). The morphologies of the samples were characterized by using FESEM (Sigma microscope, Zeiss, 20 kV), an energy dispersive X-ray detector (EDX, United Kingdom), and TEM (JEOL JEM-200CX, Japan) (JEOL-2000CX, 200 kV). The FTIR spectra were recorded on a Bruker (USA) VECTOR 22 spectrometer.

Electrochemical charge–discharge performance of the samples was evaluated in model CR2016 coin cells. The as-synthesized Sn@C films were directly used as a working electrode without binder or conductive carbon. Lithium foil was used as the counterelectrode, 1 *M* $LiPF_6$ in ethylene carbonate (EC):dimethyl carbonate (DMC) = 1:1 was used as the electrolyte, and a Celgard (Charlotte, USA) 2300 porous membrane was used as the separator. The cell was galvanostatically cycled between 0.001 and 3.0 V versus Li/Li^+ under a constant current of 75 mA g^{-1}.

RESULTS AND DISCUSSION

The preparation of Sn@C fibers from $SnCl_2$/PAN precursors, as shown in Figure 1, is mainly composed of two steps: thermal stabilization and carbonization of the PAN matrix. The first step (stabilization) involves heating the $SnCl_2$/PAN fibers under 250 °C in air atmosphere, with accompanying oxidation and cyclization of the PAN molecules. It is very important to avoid the decomposition of PAN under the subsequent high-temperature pyrolysis. During the stabilization process, PAN molecules in the composite of the $SnCl_2$/PAN film undergo a number of physical and chemical changes that convert the linear PAN molecular chains to an aromatic ladder structure suitable for further carbonization and conversion to carbon fibers. Meanwhile, $SnCl_2$ is oxidized to SnO_2 during the cyclization of PAN molecules, as shown in Figure 1(b). In the subsequent carbonization process of SnO_2/PAN at high temperature and inert

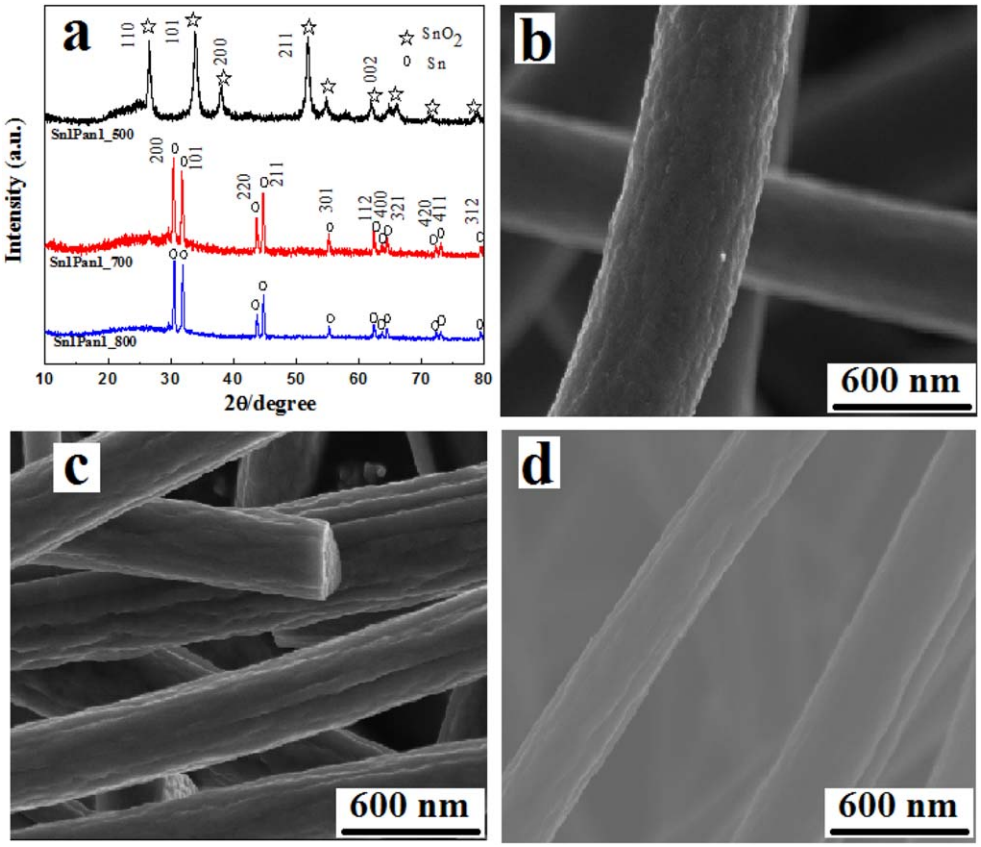

Figure 4. (a) XRD patterns, and SEM images of (b) Sn1Pan1_500, (c) Sn1Pan1_700, and (d) Sn1Pan1_800. [Color figure can be viewed in the online issue, which is available at wileyonlinelibrary.com.]

atmosphere, the polymer PAN converts to carbon fiber, while tin crystals are obtained after part of the SnO_2 has been reduced by carbon, as shown in Figure 1(c).

In the carbonization process under high temperature and inert atmosphere, the components containing N and H elements of the $SnCl_2$/PAN fibers are removed. The diameter of the fibers is decreased, but the chainlike carbon skeleton of PAN still remains. As shown in Figure 2, the FTIR spectra of the samples confirm the processes before and after carbonization. Before heat treatment, the absorption peaks of the —CN stretching vibration and —NH vibration in PAN chains are present at 2243 and 2345 cm^{-1}, respectively. The band at 1450 cm^{-1} is attributed to the symmetrical bending vibrations of $—CH_2—$. The absorption at 1626 cm^{-1} is attributed to the stretching of C=C.[35] After heat treatment at 500 °C, 700 °C, or 800 °C, the spectra indicated that the —CN band and —NH band had disappeared. The band at 1626 cm^{-1}, assigned to the stretching vibrations of C=C, moved to a new band around 1545 cm^{-1}, which results from the progress of cyclization and dehydrogenation of the PAN fibers.[36] The band around 1283 cm^{-1} corresponds to C=C bending vibrations of the carbon backbone. The vibration changes reveal that the PAN fiber has been converted to carbon. There is a new peak at around 552 cm^{-1} assigned to the vibration mode of O—Sn—O [Figure 2(a–c)], which indicates the presence of SnO_2 in the sample.

Figure 3 shows the XRD patterns and SEM images of the as-synthesized Sn@C nanofibers with weight ratio Sn3Pan2 of the precursors $SnCl_2$ and PAN, after heat treatment at 500 °C, 700 °C, or 800 °C. The component of tin is strongly dependent on the heat-treatment temperature. At the lowest temperature of 500 °C, all of the peaks in the sample Sn3Pan2_500 are assigned to those of SnO_2 (JCPDS No. 41-1445), and no reflection line corresponding to the phase of Sn can be observed.[37] Increasing the heat-treatment temperature to 700 °C, the XRD analysis of the Sn3Pan2_700 nanofibers clearly reveals a mixed diffraction pattern of SnO_2 and metallic Sn (JCPDS No. 04-0673). At the highest carbonization temperature of 800 °C, the reflection lines of the sample Sn3Pan2_800 mainly correspond to the phase of Sn. There are minor tin oxides left due to the absolute reduction by carbon at very high temperature. Meanwhile, the heat-treatment temperatures influence the fiber component and diameters of PAN, as shown in Figure 3. The presence of a broad peak around 25° [Figure 3(a)] indicates the PAN fiber converted to carbon, and the resulting carbon fiber is a hard carbon or nongraphitized carbon. After the H, N, and O elements are removed from PAN and part of the carbon is involved in the reduction of tin oxide at high temperature, the diameters of the Sn@C fibers are decreased. Along with the increased carbonization temperature from 500 °C to 800 °C, the average diameter of the fiber was reduced from 480 nm and 340 nm to 240 nm, respectively.

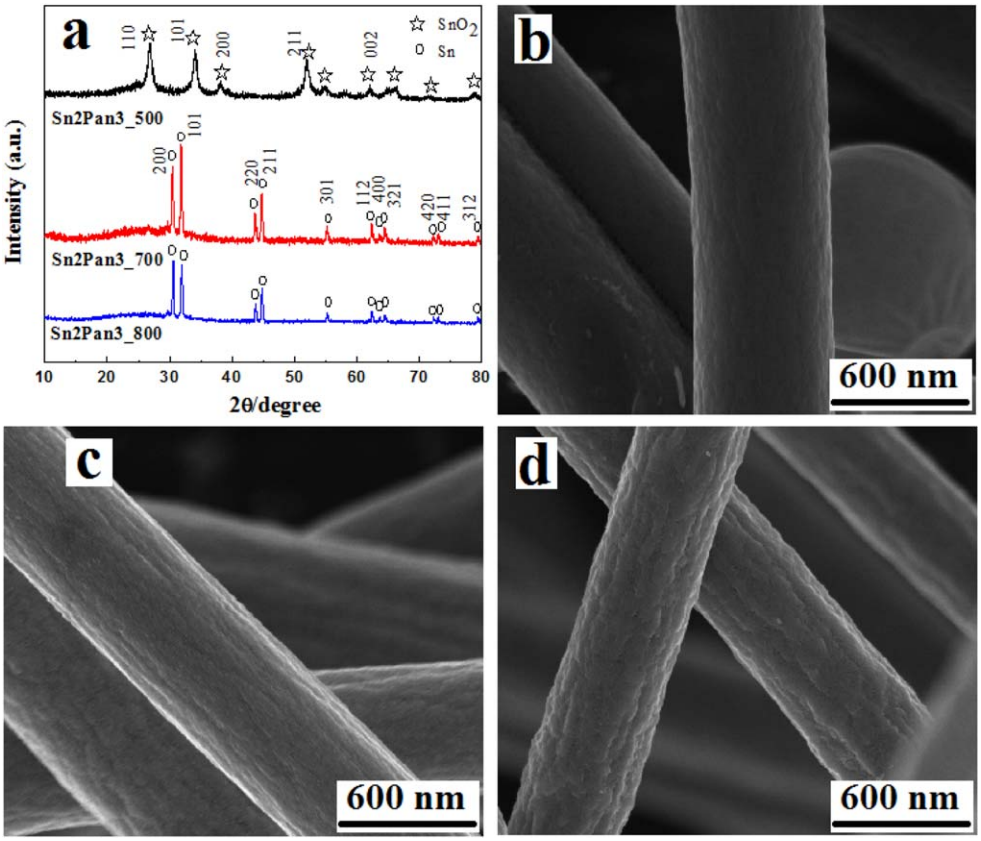

Figure 5. (a) XRD patterns, and SEM images of (b) Sn2Pan3_500, (c) Sn2Pan3_700, and (d) Sn2Pan3_800. [Color figure can be viewed in the online issue, which is available at wileyonlinelibrary.com.]

Figures 4 and 5 show the XRD patterns and SEM images of the samples Sn1Pan1 and Sn2Pan3 with increased PAN content. All the peaks in the samples treated at 500 °C are still assigned to the phase of SnO_2. Under the higher temperatures of 700 °C and 800 °C, no reflection line corresponding to the phase of SnO_2 can be observed. For the higher content of carbon in Sn1Pan1 and Sn2Pan3, SnO_2 has been absolutely reduced to metallic Sn by carbon thermal reduction. On the other hand, the diameters of the composite fibers are quite influenced by the carbonization temperature and the ratio of tin and PAN. The SEM images [Figures 4(b–d) and 5(b–d)] show that the diameter of the fiber was increased along with the increased concentration of PAN in the precursors. The average diameters of the samples are listed in Table I. Along with the increased temperature, the average diameters of the fiber are reduced because the shrinkage of the fibers is attributed to the removal of N and H elements in PAN molecules.

As listed in Table I, along with the increased concentration of tin in the precursors, the average diameters of the fibers go to smaller values. For example, the estimated diameters of the Sn@C fibers are 340, 360, and 540 nm in Sn3Pan2, Sn1Pan1, and Sn2Pan3, respectively. The morphology and diameter of polymer fibers synthesized by electrospinning are always dependent on the concentration and the additive material, because the addition of metal salts results in a higher charge density on the surface of the ejected jet during spinning.[38] In this work, tin salt plays the role of additive to adjust the morphology of as-produced fibers besides being the source of tin nanoparticles.

During the carbonization process of the SnO_2/PAN at high temperature and inert atmosphere, the polymer PAN converts to carbon fiber, while tin crystals are obtained after SnO_2 has been reduced by carbon. The morphology, crystal growth, and crystal structure of tin crystal present changes with the concentration of tin in the precursor $SnCl_2$/PAN and the heat-treatment temperature. The lattice parameters and average crystal size calculated by using the MDI Jade software are listed in Table II. It should be noted in Table II that the main phase is tin in the samples heat-treated at 700 and 800 °C listed above Sn, and the main phase is SnO_2 in the samples treated at 500 °C listed above SnO_2.

Compared with the lattice parameters of pure metal tin and SnO_2, Sn1Pan1_700 presents lattice parameters similar to those

Table I. Calculated Average Diameters of the Composite Fibers before and after Heat Treatment

Samples	Sn3Pan2	Sn1Pan1	Sn2Pan3
Before	570 nm	710 nm	900 nm
500 °C	480 nm	540 nm	600 nm
700 °C	340 nm	360 nm	540 nm
800 °C	240 nm	300 nm	460 nm

Table II. Calculated Lattice Parameters and the Average Crystal Size of the As-Synthesized Samples

	Lattice parameters				
Samples	*a* (Å)	*c* (Å)	*c*/*a*	V_{cell} (Å^3)	XS (nm)
Sn3Pan2_700	5.84355	3.19054	0.5460	108.95	13.6
Sn3Pan2_800	5.80972	3.17009	0.5457	107.0	19.1
Sn1Pan1_700	5.83146	3.17941	0.5452	108.12	58.3
Sn1Pan1_800	5.82914	3.18118	0.5457	108.09	84.9
Sn2Pan3_700	5.84281	3.18906	0.5458	108.87	53.5
Sn2Pan3_800	5.84192	3.18676	0.5455	108.76	70.6
Sn	5.831	3.182	0.5457	108.19	—
Sn3Pan2_500	4.7417	3.2001	0.6744	72.08	22.5
Sn1Pan1_500	4.73244	3.17065	0.6700	71.01	14.8
Sn2Pan3_500	4.72677	3.15225	0.6669	70.43	11.2
SnO_2	4.7382	3.1871	0.6726	71.55	—

The data are referred from JCPDS 04-0673 and JCPDS No. 41-1445. XS: Calculated average crystal size using MDI Jade software.

of metal tin (PDF No. 04-0673). Sn3Pan2_500 presents lattice parameters similar to those of SnO_2 (JCPDS No. 41-1445). Moreover, the crystal size of Sn and SnO_2 in the samples is strongly affected by the tin concentration in the precursors and the heat-treatment temperature. The average crystallite sizes (XS) of the samples are increased along with the increased concentration of tin and the increased heat-treatment temperature. For example, Sn2Pan3, with the lowest tin content, presents average crystallite sizes of 11.2, 53.5, and 70.6 nm after carbonization at 500, 700, and 800 °C, respectively. A higher

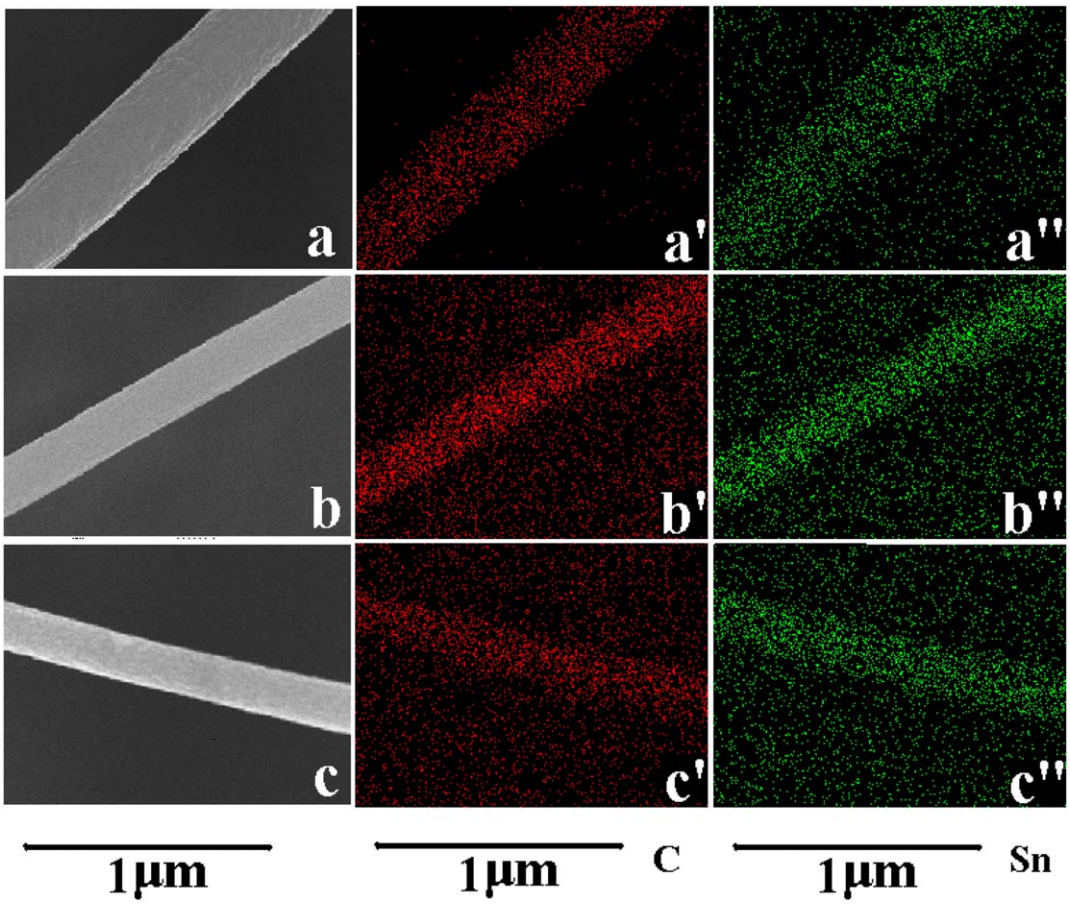

Figure 6. SEM images and elemental mapping of C and Sn: (a,a′,a″) Sn1Pan1_500, (b,b′,b″) Sn1Pan1_700, (c,c′,c″) Sn1Pan1_800. [Color figure can be viewed in the online issue, which is available at wileyonlinelibrary.com.]

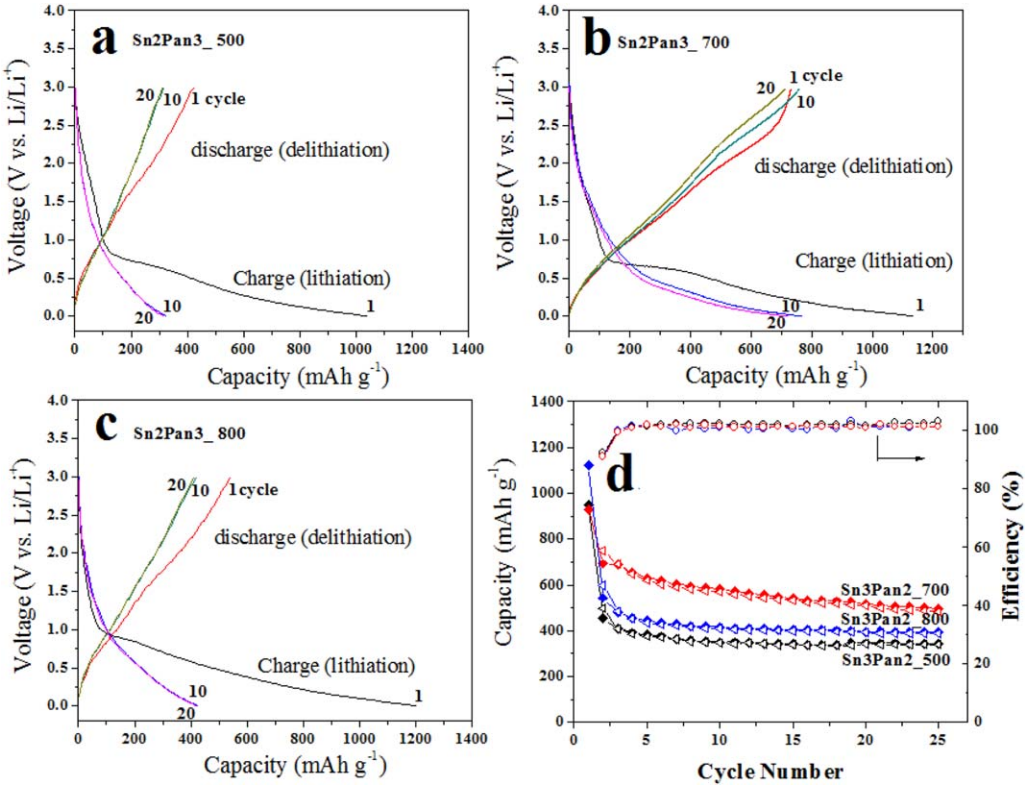

Figure 7. The specific charge/discharge profiles, cycle performance, and coulombic efficiency of Sn3Pan2. The samples with three heat-treatment temperatures are listed in the figures. [Color figure can be viewed in the online issue, which is available at wileyonlinelibrary.com.]

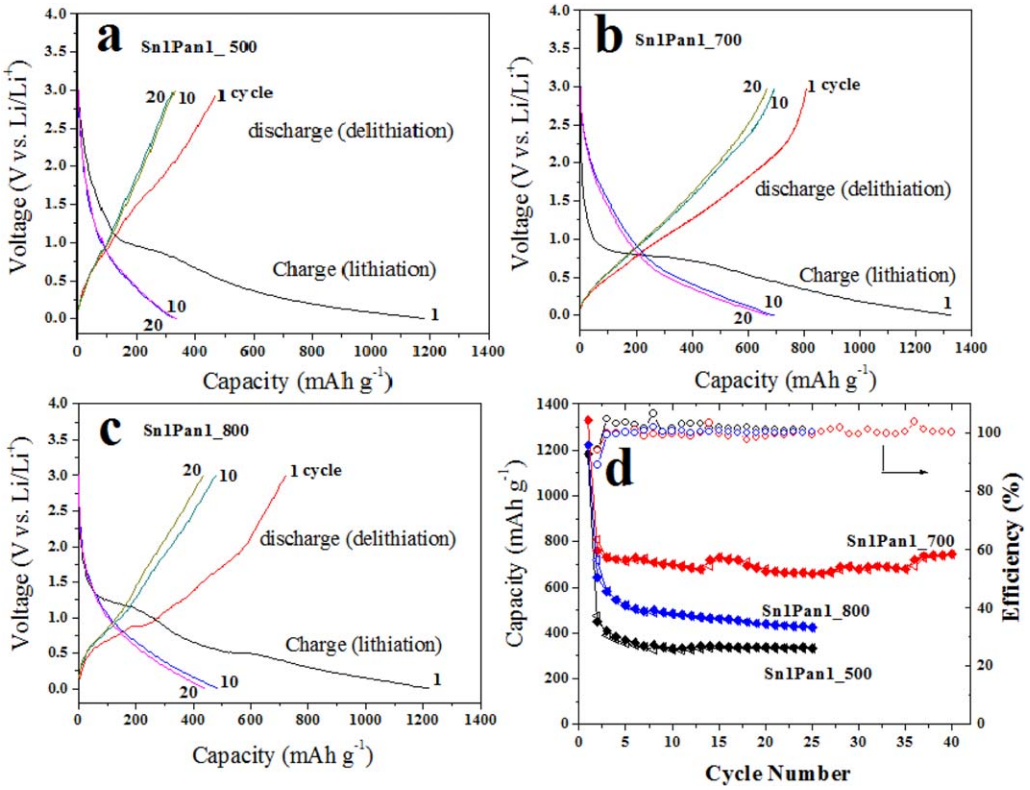

Figure 8. The specific charge/discharge profiles, cycle performance, and coulombic efficiency of Sn1Pan1. The samples with three heat-treatment temperatures are listed in the figures. [Color figure can be viewed in the online issue, which is available at wiley onlinelibrary.com.]

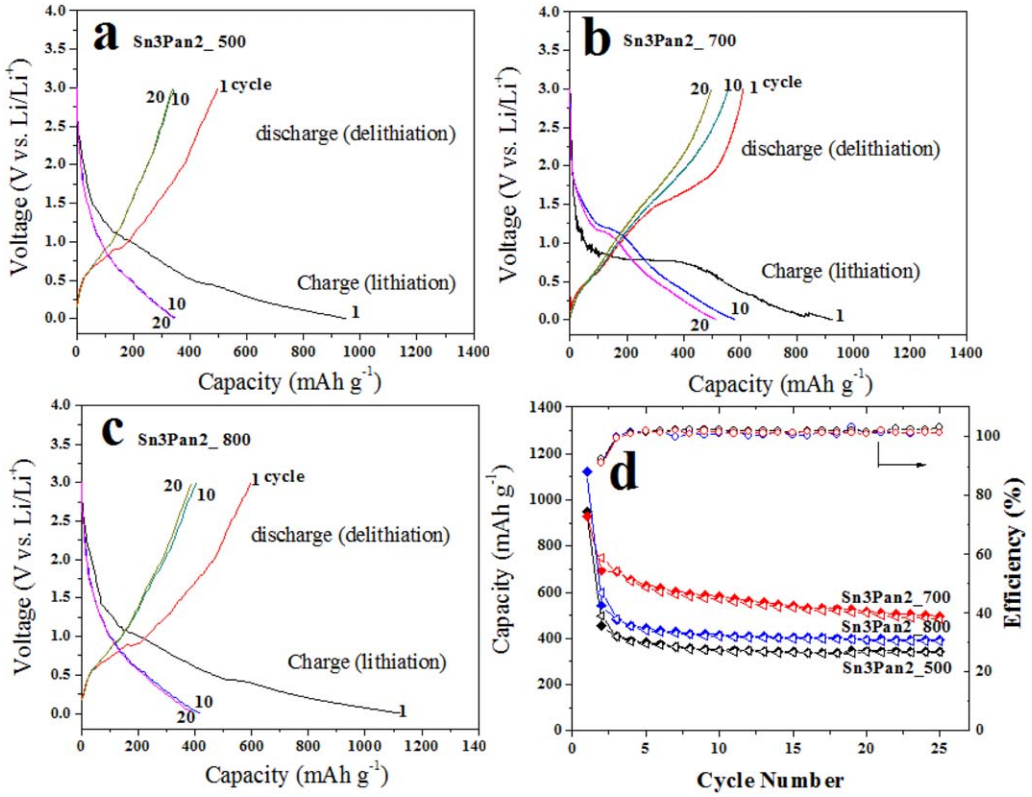

Figure 9. The specific charge/discharge profiles, cycle performance, and coulombic efficiency of Sn2Pan3. The samples with three heat-treatment temperatures are listed in the figures. [Color figure can be viewed in the online issue, which is available at wileyonlinelibrary.com.]

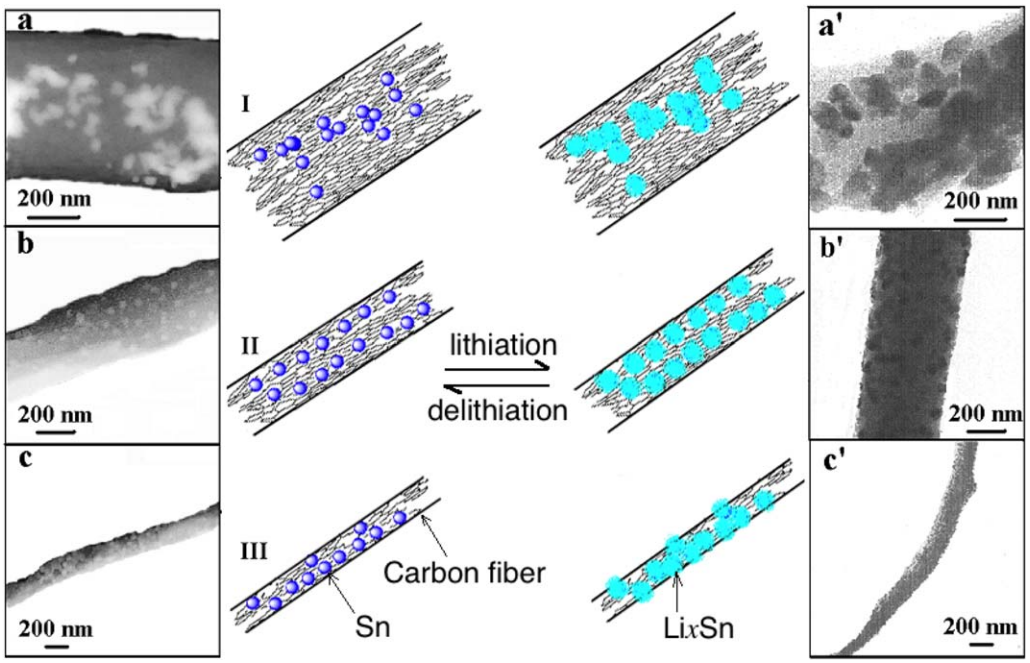

Figure 10. Left and right: TEM images of Sn1Pan1 before (a–c) and after (a′–c′) lithiation/delithiation, in which (a) and (a′) are Sn1Pan1_500, (b) and (b′) are Sn1Pan1_700, and (c) and (c′) are Sn1Pan1_800. Center: the schematic composite structures where nanocrystallites are wrapped in the carbon fibers: (I) smaller nanocrystallites in coexistence with bigger diameter fibers, (II) proper morphology of nanocrystallites in homogeneous coexistence with carbon fiber, and (III) bigger nanocrystallites in coexistence with smaller diameter fiber. [Color figure can be viewed in the online issue, which is available at wileyonlinelibrary.com.]

carbonization temperature leads to the crystallites of tin growing bigger. But at the high carbonization temperature of 800 °C, the microstructure of Sn@C with the enlarged tin nanoparticles and smaller carbon fibers results in a decrease in the void zone for anode materials during lithiation and delithiation.

The charge/discharge profiles and cycle performance of Sn3Pan2 carbonized at various temperatures are shown in Figure 6. The voltage profile of the composite electrode exhibits the typical characteristics of a Sn-containing electrode. Three voltage ranges, 3.0–0.8, 0.8–0.3, and 0.3–0.0 V, versus Li^+/Li are observed in the initial discharge curves. The first is attributed to the formation of a solid electrolyte interphase (SEI) film, and the last two curves correspond to the electrochemical lithiation of Li and Sn. Sn3Pan2_700 delivers the initial specific capacity of 929.2 mAh g^{-1}. The large initial capacity loss of the Sn@C fiber electrode is partly attributed to the formation of an SEI layer.[39–41]

Figures 7 and 8 present the electrochemical performances of Sn1Pan1 and Sn2Pan3 with lower tin content. In comparison, the samples of Sn3Pan2_700, Sn1Pan1_700, and Sn2Pan3_700 carbonized at 700 °C deliver initial discharge capacities of 929.2, 1329.8, and 1137.0 mAh g^{-1}, respectively. The samples Sn1Pan1_700 and Sn2Pan3_700 present higher initial discharge capacities than Sn3Pan2_700, which contains two phases of Sn and SnO_2, because metallic tin delivers higher theoretical capacities (990 mAh g^{-1}) than SnO_2 (790 mAh g^{-1}). In the following charge process, the charge capacities are 611.1, 808.6, and 731.4 mAh g^{-1} in the samples Sn3Pan2_700, Sn1Pan1_700, and Sn2Pan3_700, respectively. The carbonization is beneficial for the formation of tin-containing nanoparticles wrapped in carbon fibers, and the proper temperature improves the carbonization extent of PAN and the formation of tin. On the other hand, the precursor content of the sample is also one of the factors in electrochemical performance. For example, the initial discharge capacities are 1184.0, 1329.8, and 1221.7 mAh g^{-1} in the samples of Sn1Pan1 (Figure 9) carbonized at 500, 700, and 800 °C, respectively. In the subsequent charge process, the charge capacities are 473.5, 808.6, and 720.2 mAh g^{-1} in Sn1Pan1_500, Sn1Pan1_700, and Sn1Pan1_800, respectively.

Regarding the cycle performance and coulomb efficiency [Figures 6(d) to 8(d)], the coulomb efficiency is near 100% except in the initial charge/discharge. The samples of Sn1Pan1_700 and Sn2Pan3_700 with lower tin content present good discharge capacity and cycle performance. For example, Sn1Pan1_700 retains a capacity of 741.1 mAh g^{-1} after 40 cycles. In several previous reports,[42,43] the reversible capacities of tin were soon decreased if the Sn particles were aggregated during lithiation/delithiation processes. The as-synthesized Sn@C composites have the advantage that the aggregations of metal or metal oxide enwrapped in carbon fibers are weakened during the charging and discharging processes.

Figure 9 covers the entire area of the nanofiber. The composite structure of tin nanoparticles dispersed and limited inside the carbon fibers has several advantages. First, the carbon fibers provide a higher specific surface area, good electrical contact, and good lithium ion conductivity; second, the adequate void space (as a "buffer zone") in the carbon fibers flexibly accommodates the large volume change in the lithiation and delithiation processes.[39,41] The relatively separated tin nanoparticles inside the carbon fibers retarded the aggregation during the Li alloying accompanying the volume change, leading to good cycle performance. Figure 10 shows the TEM images of the as-synthesized samples Sn1Pan1 and the sketch of the microstructure of tin-containing nanoparticles wrapped in carbon fibers before and after discharge. Lower heat-treatment temperatures and tin concentration result in smaller crystals and bigger fiber diameters, which appear in the aggregation during the charging and discharging processes [as shown in Figure 10(I)]. Higher heat-treatment temperatures and a higher tin content in the samples lead to bigger crystals and smaller fiber diameters, which is not beneficial for lithiation and delithiation of Sn@C, due to the smaller "buffer zone" provided by shrunken carbon fibers [as shown in Figure 10(III)]. The proper heat-treatment temperatures and proper concentration of tin in samples will produce a good morphology of nanocrystallites coexisting with carbon fibers, which improves the electrochemical performance of the samples [Figure 10(II)].

CONCLUSIONS

A series of one-dimensional nanostructural samples of tin-containing nanoparticles wrapped in carbon nanofibers are synthesized. The diameters of the carbon fibers and the size of the wrapped nanoparticles are carefully modeled. The particle size and fiber diameters of the samples change with the precursor content and carbonization temperature, which play key roles in the electrochemical performance. The sample Sn1Pan1_700 delivers the initial capacity of 1329.8 mAh g^{-1} and remains at 741.1 mAh g^{-1} at the 40th cycle. The proper morphology of tin nanoparticles wrapped in carbon fibers presents the best specific capacity and cyclic performance, because proper structure of the carbon fiber hinders the aggregation of tin nanoparticles during lithiation/delithiation processes.

ACKNOWLEDGMENTS

The work was sponsored by NSF of China (Grant No. 51172032, 51203013).

REFERENCES

1. Aldon, L.; Garcia, A.; Olivier-Fourcade, J.; Jumas, J.-C.; Fernandez-Madrigal, F. J.; Lavela, P.; Vicente, C. P.; Tirado, J. L. *J. Power Sources* **2003**, *119*, 585.
2. Choi, N.-S.; Yao, Y.; Cui, Y.; Cho, J. J. *J. Mater. Chem.* **2011**, *21*, 9825.
3. Hamon, Y.; Brousse, T.; Jousse, F.; Topart, P.; Buvat, P.; Schleich, D. M. *J. Power Sources.* **2001**, *97*, 185.
4. Courteny, I. A.; Dahn, J. R. *J. Electrochem. Soc.* **1997**, *144*, 2045.
5. Winter, M.; Besenhard, J. O. *Electrochim. Acta.* **1999**, *45*, 31.
6. Wachtler, M.; Besenhard, J. O.; Winter, M. *J. Power Sources* **2001**, *94*, 189.
7. Kang, H. K.; Lee, S. R.; Cho, W. I.; Cho, B. W. *Phys. Chem. Chem. Phys.* **2013**, *15*, 1569.

8. Wang, G. X.; Sun, L.; Bradhurst, D. H.; Zhong, S.; Dou, S. X.; Liu, H. K. *J. Alloys Compd.* **2000**, *306*, 249.
9. Weydanz, W. J.; Wohlfahrt-Mehrens, M.; Huggins, R. A. *J. Power Sources* **1999**, *81*, 237.
10. Wolfenstine, J. *J. Power Sources* **2003**, *124*, 241.
11. Roberts, G. A.; Cairns, E. J.; Reimer, J. A. *J. Power Sources* **2002**, *110*, 424.
12. Tan, C. H.; Qi, G. W.; Li, Y. P.; Guo, J.; Wang, X.; Kong, D. L; Wang, H. J.; Zhang, S. Y. *Int. J. Electrochem. Sci.* **2013**, *8*, 1966.
13. Yao, J. H.; Zhang, P. J.; Shen, C. Q.; Aguey-Zinsou, K. F.; Wang, L. B. *Ionics* **2013**, *19*, 295; https://vpn0.shu.edu.cn/prx/000/http/apps.webofknowledge.com/OneClickSearch.do?product=UA &search_mode=OneClickSearch &excludeEventConfig=ExcludeIfFromFullRecPage &colName=INSPEC &SID=3AbPRV9oo8TTQST9zFQ &field=AU &value=Jinhan +Yao &cacheurlFromRightClick=no.
14. Guo, H.; Zhao, H. L.; Yin, C. L.; Qiu, W. H. *J. Alloys Compd.* **2006**, *426*, 277.
15. Reddy, M. V.; Tse, L. Y.; Ke, W.; Bruce, Z.; Chowdari, B. V. R. *Mater. Lett.* **2015**, *138*, 231.
16. Li, J.; Ru, Q.; Hu, S. J.; Sun, D. W.; Zhang, B. B.; Hou, X. H. *Electrochim. Acta* **2013**, *113*, 505.
17. Birrozzi, A.; Raccichini, R.; Nobili, F.; Marinaro, M.; Tossici, R.; Marassi, R. *Electrochim. Acta* **2014**, *137*, 228.
18. Rai, A. K.; Thi, T. V.; Paul, B. J.; Kim, J. *Electrochim. Acta* **2014**, *146*, 577.
19. Wang, J.; Zhao, H. L.; Zeng, Z. P.; Lv, P. P.; Li, Z. L.; Zhang, T. H.; Yang, T. R. *Mater. Chem. Phys.* **2014**, *148*, 699.
20. Wu, J. B.; Zhu, Z. W.; Zhang, H. W.; Fu, H. M.; Li, H.; Wang, A. M.; Zhang, H. F.; Hu, Z. Q. A. *J. Alloys Compd.* **2014**, *596*, 86.
21. Wu, J.; Chen, C. H.; Hao, Y.; Wang, C. L. *Colloids Surf., A* **2015**, *468*, 17.
22. Wu, X. Y.; Ma, J.; Hu, Y. S.; Li, H.; Chen, L. G. *J. Energy Chem.* **2014**, *23*, 269.
23. Yang, J.; Winter, M.; Besenhard, J. O. *Solid State Ionics* **1996**, *90*, 281.
24. Wang, H.; Pan, Q. M.; Cheng, Y. X.; Zhao, J. W.; Yin, G. P. *Electrochim. Acta* **2009**, *54*, 2851.
25. Xu, Y. H.; Liu, Q.; Zhu, Y. J.; Liu, Y. H.; Langrock, A.; Zachariah, M. R.; Wang, C. S. *Nano Lett.* **2013**, *13*, 470.
26. Chen, P. C.; Xu, J.; Chen, H. T.; Zhou, C. W. *Nano Res.* **2011**, *4*, 290.
27. Oh, S. M.; Myung, S. T.; Jang, M. W.; Scrosati, B.; Hassoun, J.; Sun, Y. K. *Phys. Chem. Chem. Phys.* **2013**, *15*, 3827.
28. Yang, Z. C.; Guo, J. C.; Xu, S. M.; Yu, Y. C.; Abruña, H. D.; Archera, L. A. *Electrochem. Commun.* **2013**, *28*, 40.
29. Zhou, W. C.; Upreti, S. M.; Whittingham, S. *Electrochem. Commun.* **2011**, *13*, 158.
30. Wang, Z. H.; Han, Z.; Geng, D. Y.; Zhang, Z. D. *Chem. Phys. Lett.* **2010**, *489*, 187.
31. Hsu, K. C.; Liu, C. E.; Chen, P. C.; Lee, C. Y.; Chiu, H. T. *J. Mater. Chem.* **2012**, *22*, 21533.
32. Wang, Y. G.; Li, B.; Zhang, C. L.; Tao, H.; Kang, S. F.; Jiang, S.; Li, X. *J. Power Sources* **2012**, *219*, 89.
33. Wang, H. Y.; Huang, H. Q.; Chen, L.; Wang, C. G.; Yan, B.; Yu, Y. T.; Yang, Y.; Yang, G. *ACS Sustainable Chem. Eng.* **2014**, *2*, 2310.
34. Wang, H. Y.; Gao, P.; Lu, S. F.; Liu, H. D.; Yang, G.; Pinto, J.; Jiang, X. F. *Electrochim. Acta* **2011**, *58*, 44.
35. Dalton, S.; Heatley, F.; Budd, P. M. *Polymer* **1999**, *40*, 5531.
36. Rahaman, M. S. A.; Ismail, A. F.; Mustafa, A. *Polym. Degrad. Stabil.* **2007**, *92*, 1421.
37. Veeraraghavan, B.; Durairajan, A.; Haran, B.; Popov, B.; Guidotti, R. J. *Electrochem. Soc.* **2002**, *149*, A675.
38. Zong, X. H.; Kim, K.; Fang, D. F.; Ran, S. F.; Hsiao, B. S.; Chu, B. *Polymer* **2002**, *43*, 4403.
39. Shembel, E.; Apostolova, R.; Nagirny, V.; Kirsanova, I.; Grebenkin, P.; Lytvyn, P. J. *Solid State Electrochem.* **2005**, *9*, 96.
40. Yu, Y.; Gu, L.; Wang, C.; Dhanabalan, A.; Aken, P. A. *Angew. Chem. Int. Ed.* **2009**, *48*, 6485.
41. Yu, Y. H.; Yang, Q.; Teng, D. H.; Yang, X. P.; Ryu, S. *Electrochem. Commun.* **2010**, *12*, 1187.
42. Wang, Y.; Zeng, H. C.; Lee, J. Y. *Adv. Mater.* **2006**, *18*, 645.
43. Shembel, E.; Apostolova, R.; Nagirny, V.; Kirsanova, I.; Grebenkin, P.; Lytvyn, P. *J. Solid State Electrochem.* **2005**, *9*, 96.
44. Grugeon, S.; Laruelle, S.; Herrera-Urbina, R.; Dupont, L.; Poizot, P.; Tarascon, J. M. *J. Electrochem. Soc.* **2001**, *148*, A285.